Sustainable Energy & Fuels

ROYAL SOCIETY OF CHEMISTRY

PAPER

View Article Online
View Journal

Cite this: DOI: 10.1039/d2se01522f

Energy level modulation of TiO_2 using amino trimethylene phosphonic acid for efficient perovskite solar cells with an average V_{OC} of 1.19 V†

Xiaopeng Yue,[ab] Bingbing Fan,[a] Xing Zhao,[a] Yingying Yang,[a] Shujie Qu,[a] Qiang Zhang,[a] Xin Sun,[a] Peng Cui,[a] Junfeng Ma[a] and Meicheng Li *[a]

The performance of planar perovskite solar cells (PSCs) is closely linked to the charge extraction and transfer in electron transporting layers (ETLs). To achieve a good control of the photoelectric properties of TiO_2 ETLs, we introduce amino trimethylene phosphonic (ATMP) acid into the chemical bath deposition (CBD) process of TiO_2 films. ATMP can effectively control the crystal growth of TiO_2 particles to get an optimized ETL with preferable band energy and surface topography, which is beneficial for the energy level alignment and interface contact between the ETL and perovskite active layer. Compared to the control devices, the open circuit voltage (V_{OC}) of PSCs with ATMP–TiO_2 is increased from 1.17 V to 1.19 V, achieving a higher average power conversion efficiency (PCE) of 24.10%. The enhanced performance of ATMP–TiO_2 PSCs is attributed to suppressed defects and well-matched energy level alignment at the perovskite/ETL interface, efficiently facilitating charge carrier extraction and electron transport. This work sheds light on designing an efficient ETL by tuning the precursor solution with environmental and inexpensive modifiers toward PSCs exhibiting outstanding performances.

Received 1st November 2022
Accepted 14th December 2022

DOI: 10.1039/d2se01522f

rsc.li/sustainable-energy

Introduction

Organic–inorganic lead halide perovskites have attracted tremendous attention as light sensitive materials in photovoltaic devices due to their excellent optoelectronic properties such as strong visible light absorbance, low exciton binding energy, and long charge carrier diffusion length.[1–5] The power conversion efficiency (PCE) of planar perovskite solar cells (PSCs) has been increased beyond 25% in the past few years, demonstrating the great potential for commercialization.[6–9] Besides improvements in perovskite absorbers, development of efficient electron transport layers (ETLs) is another important factor that contributes to the revolutionary efficiency growth.[10–14] In conventional planar-structured PSCs, the ETL is deposited onto a transparent conductive electrode, extracting photogenerated electrons from the perovskite layer and transporting them to the charge collection electrode.[15,16] The film quality and energy level of ETLs play an important role in determining charge extraction/transfer at the ETL/perovskite interface and thus influence the photovoltaic performance.

With the advantage of low-cost, excellent chemical stability and band edge levels matching with those of perovskites, titanium dioxide (TiO_2) is one of the commonly utilized ETLs in PSCs. Generally, high-temperature sintering treatment is essential to improve the crystallinity and conductivity of traditional TiO_2 ETLs. Fortunately, several low-temperature chemical bath deposition (CBD) methods have been reported to prepare efficient TiO_2 ETLs for PSCs, giving a cost-effective solution to fabricate TiO_2 ETLs which can be applied in industrial scales.[17–22] To further improve the electron extraction and transport at the TiO_2/perovskite interface, various strategies such as element doping, introduction of a heterojunction layer and surface modifications have been developed to optimize the TiO_2 films.[17,23–27] For instance, Zhou *et al.* reported the utilization of Y-doped TiO_2 processed at temperatures below 150 °C as an efficient ETL, delivering high efficiency and a suppressed hysteresis phenomenon in comparison with the undoped device.[25] Petrozza's group inserted a fullerene derivative (60-PCBM) layer between the TiO_2 ETL and perovskite absorber to achieve improved charge extraction and high steady-state efficiency for planar PSCs.[28] As for the latter method, $TiCl_4$ treatment has been most frequently reported to ameliorate the surface properties of TiO_2 and TiO_2/perovskite interface.[23,24] Besides, a certain number of phosphonic acids (PAs) can work as interfacial modifiers to optimize electrical contacts between the TiO_2 ETL and active layers.[29] Tao *et al.* used phosphonic acids to systematically modulate the surface properties and interfacial energy barrier by changing the chain length and

[a]State Key Laboratory of Alternate Electrical Power System with Renewable Energy Sources, School of New Energy, North China Electric Power University, Beijing 102206, China. E-mail: mcli@ncepu.edu.cn

[b]School of Energy and Environmental Engineering, Hebei University of Engineering, Handan, Hebei 056038, China

† Electronic supplementary information (ESI) available. See DOI: https://doi.org/10.1039/d2se01522f

terminal functional group on PAs.[30] PSCs with 4,4,4-trifluorobutylphosphonic acid (TFBPA)-modified TiO_2 harvest the highest efficiency with reduced hysteresis due to the improved charge extraction and carrier balance in the device. Extensive research on these effective post-treatment strategies indicates that there is much room for further improvement of the as-prepared TiO_2 layer. It is necessary to explore efficient TiO_2 ETL fabrication methods with simpler operation and lower cost.[18,22]

Herein, we developed an efficient TiO_2 ETL through introducing amino trimethylene phosphonic acid (ATMP) into a titanium tetrachloride ($TiCl_4$) aqueous solution. ATMP can chelate with Ti^{4+} and bind with TiO_2 particles to adjust the crystal growth and hinder the aggregation of TiO_2, resulting in efficient TiO_2 ETLs with appropriate band energy and surface morphology. In comparison with the control device, PSCs with ATMP–TiO_2 deliver an increased open circuit voltage (V_{OC}) of 1.19 V, achieving an average PCE of 24.10%. The improvement in the photovoltaic performance of the ATMP–TiO_2 device is attributed to the better energy band alignment at the ATMP–TiO_2/perovskite interface and modified electrical properties of the TiO_2 ETL, which is beneficial to accelerate charge extraction and suppress charge recombination. This work provides a simple and efficient way to fabricate TiO_2 ETLs for high-efficiency PSCs.

Results and discussion

The molecular structure of ATMP is shown in Fig. S1.† ATMP exhibits strong metal ion-chelation ability in aqueous solution as there are up to six bonding sites on its phosphonate groups.[29] Thus, ATMP can form a chelate complex with Ti^{4+} to adjust the crystallization of TiO_2 in the chemical bath deposition (CBD) process. Fig. 1a displays a possible structure of the Ti–ATMP chelate. The ETLs fabricated without and with ATMP are represented as TiO_2 and ATMP–TiO_2, respectively. The hydrodynamic radii of TiO_2 particles were determined by conducting dynamic light scattering (DLS) measurements on a freshly prepared reaction solution after the CBD process. As shown in Fig. 1b and c, the average particle size is 101 nm for TiO_2 and 53 nm for ATMP–TiO_2, indicating that ATMP–TiO_2 exhibits smaller size distribution compared with the control TiO_2 particles. The transmittance spectra of TiO_2 and ATMP–TiO_2 films are shown in Fig. 1c. Both control and ATMP-modified TiO_2 films deposited on FTO/glass substrates show good transmittance in the visible light range. Besides, the absorption edge of the ATMP–TiO_2 film exhibits an apparent blue shift, suggesting the increased band gap of ATMP–TiO_2 particles with smaller size.[31] The growth mechanism of ATMP–TiO_2 particles is shown in Fig. 1d. Besides undergoing chelation with Ti^{4+}, ATMP can be absorbed onto the active sites at the TiO_2 surface during the crystal growth process which will increase the repulsion between particles and hinder their agglomeration, resulting in smaller TiO_2 particles.[29,32,33]

The electronic properties of the TiO_2 films were characterized by ultraviolet photoelectron spectroscopy (UPS). As shown in Fig. 2a–c, the work function (E_F) of the ATMP–TiO_2 film is calculated to be −4.53 eV by linear extrapolation of the secondary electron cutoff, which is slightly higher than that of control TiO_2 (−4.58 eV). In addition, the difference between E_F and the valence band maximum energy (E_{VBM}) value of the ETL increases from 2.81 to 2.91 eV with ATMP incorporation. The corresponding Tauc plots are shown in Fig. S2b and c† and the band gaps of control TiO_2 and ATMP–TiO_2 films are determined to be 3.20 and 3.51 eV, respectively. As a result, the conduction band energy (E_{CB}) is calculated to be −4.19 and −3.93 eV for TiO_2 and ATMP–TiO_2, respectively (Fig. 2a). The result shows that the conduction band of ATMP–TiO_2 moves closer to that of the perovskite to facilitate the charge transport and suppressed charge recombination.[34,35] Furthermore, we applied Kelvin probe force microscopy (KPFM) to investigate the surface potential to get a deeper insight into the electronic difference between TiO_2 and ATMP–TiO_2 films. As shown in Fig. 2d and e, the average surface potential difference value of ATMP–TiO_2

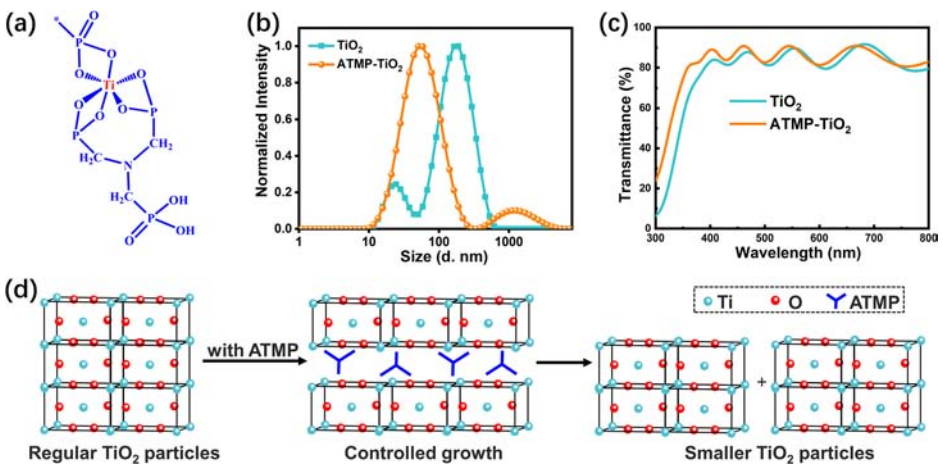

Fig. 1 (a) Possible structure of the Ti–ATMP chelate. (b) Dynamic light scattering of TiO_2 and ATMP–TiO_2 nanoparticles. (c) Transmittance spectra of TiO_2 and ATMP–TiO_2 films. (d) Growth mechanism of ATMP–TiO_2 particles.

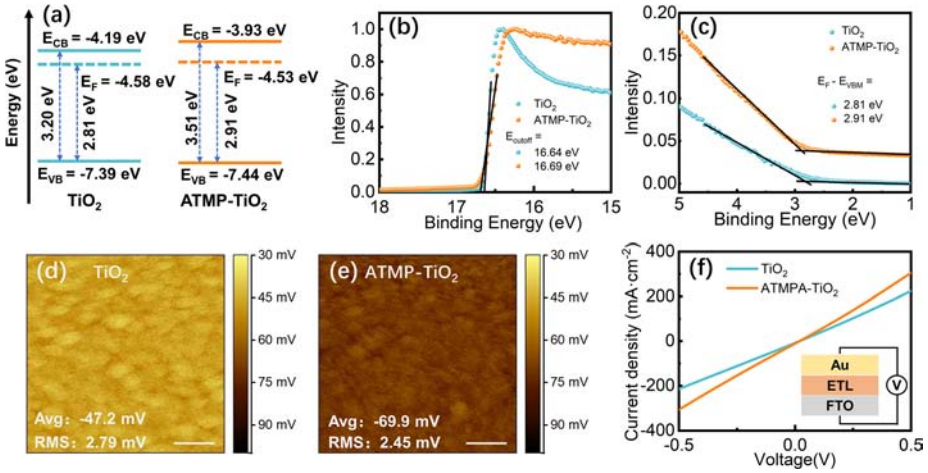

Fig. 2 (a) Schematic energy level diagrams for TiO_2 and ATMP–TiO_2 films. (b and c) UPS profiles of TiO_2 and ATMP–TiO_2 films. KPFM (5 μm × 5 μm) of (d) TiO_2 and (e) ATMP–TiO_2 films. (f) Characterization of conductivity for TiO_2 and ATMP–TiO_2 films.

decreases from −47.2 to −69.9 mV, indicating a more N-type nature of the ATMP–TiO_2 surface. Besides, the root mean square (RMS) values of the surface potential are 2.79 and 2.45 mV for TiO_2 and ATMP–TiO_2, respectively, revealing that the surface potential of the target TiO_2 film exhibits better homogeneity compared to the control one. Additionally, the ATMP–TiO_2 film exhibits better electrical conductivity compared with control TiO_2 (Fig. 2f), which is beneficial to the charge transfer at the cathode.

Undoubtedly, the topography of ETLs plays an important role in affecting the device performance. We carried out atomic force microscopy (AFM) and scanning electron microscopy (SEM) to explore the influence of ATMP on TiO_2 film topography. The 3D AFM height images are shown in Fig. 3a and d. The RMS roughness of the ATMP–TiO_2 film is 32.01 nm, which is much smaller than that of the control TiO_2 film (RMS = 51.27 nm). Because of the smoother and more homogeneous topography, ATMP–TiO_2 is supposed to form a better connection with the perovskite active layer, benefiting carrier extraction, charge transport and defect passivation at the interface. Both TiO_2 ETLs can completely cover the top surface of FTO (Fig. 3b and e), indicating effective hole-blocking and electron transport at the cathode. However, the control TiO_2 film is composed of needle-like nanoclusters and several highlight spots that appear widely dispersed on its surface SEM image, implying that bulges are caused by the agglomeration of TiO_2 particles. With ATMP incorporated in the CBD process, the obtained ATMP–TiO_2 film is more compact with less clusters (Fig. 3e), suggesting the ATMP-induced inhibition of crystal particle aggregation. The top-surface and cross-section SEM images for TiO_2 and ATMP–TiO_2 films at various chemical bath times are displayed in Fig. S3 and S4.† At the bath time of 30 min (Fig. S3a and e†),

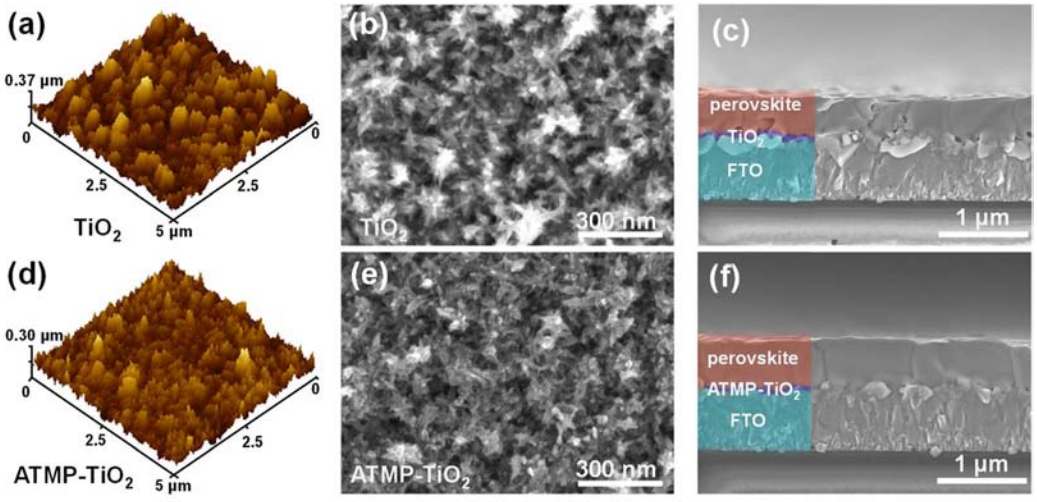

Fig. 3 3D AFM images of (a) TiO_2 and (d) ATMP–TiO_2 films. Top SEM images of (b) TiO_2 and (e) ATMP–TiO_2 films. Cross-sectional SEM images of perovskite films deposited on (c) TiO_2 and (f) ATMP–TiO_2 films.

control TiO_2 has formed a continuous film while ATMP–TiO_2 just begins to deposit on the surface of the transparent conductive substrate. When the bath time is longer than 30 min, the TiO_2 films show severer aggregation and ATMP–TiO_2 films cover the FTO surface gradually (Fig. S4†). The quite different film deposition processes of TiO_2 and ATMP–TiO_2 indicate that the chelation reaction between ATMP and titanium ion can slow down the nucleation and hinder the excessive aggregation of TiO_2 particles. X-ray photoelectron spectrometry (XPS) was measured to analyze the chemical properties of TiO_2 films. The full XPS spectrum is shown in Fig. S5a† and the presence of ATMP on the ATMP-modified TiO_2 film is confirmed by the small peak of phosphorus (P) core level emissions occurring at the binding energy of 133.3 eV (P 2p) (Fig. S5b†).[36] As shown in Fig. S5c,† there is no difference between the peak position of Ti 2p spectra for TiO_2 and ATMP–TiO_2 films. In comparison with control TiO_2, ATMP–TiO_2 exhibits an enhanced shoulder peak at a higher binding energy in the O 1s spectra (Fig. S5d†), which is related to oxygen in the phosphonate groups, further confirming the presence of ATMP in the target TiO_2 layer.

Afterward, SEM and X-ray diffraction (XRD) were measured to study the surface morphology and crystallinity of perovskite active layers deposited on TiO_2 and ATMP–TiO_2 films. The cross-section SEM images of perovskite film are shown in Fig. 3c and f. There is no big difference in the top-surface morphology of the perovskite as shown in Fig. S6.† In Fig. 3c, the cross-section of the perovskite film fabricated on the control TiO_2 substrate displays plenty of grain boundaries, which would act as charge traps and cause severe recombination along with energy loss. With ATMP regulation (Fig. 3f), the decreased gain boundaries and disappeared pinholes prove the improved film quality, which can facilitate the electron carrier extraction and charge transport. Besides, the defects at the ETL/perovskite interface caused by the inferior bulges can be observed, especially for the control sample. Fig. S7† shows the XRD patterns of perovskite films deposited on TiO_2 and ATMP–TiO_2 ETLs. The peaks located at 14.2°, 20.1°, 28.3° and 40.2° are assigned to the (100), (112), (200) and (224) crystal planes, respectively, in which (100) is the most balanced and stable plane.[37] The dominant plane is (224) for the TiO_2 based perovskite film and it shifts to (100) for perovskite deposited on the ATMP–TiO_2 substrate, indicating the optimized crystallinity of the target perovskite film which is well-consistent with the SEM analysis.

To investigate the influence of different ETLs on the PSC photovoltaic performance, we fabricated devices with the structure of glass/FTO/TiO_2 or ATMP–TiO_2/perovskite/spiro-OMeTAD/Au. The photovoltaic performance of PSCs based on different ETLs was measured under AM 1.5G illumination with an intensity of 100 mW cm^{-2}. The statistics (in total 8 devices from one batch) of V_{OC}, J_{SC}, fill factor (FF) and PCE are plotted in Fig. 4a–d. And the corresponding photovoltaic performance parameters are summarized in Table 1. The control device displays an average J_{SC} of 24.59 mA cm^{-2}, a V_{OC} of 1.17 V and an FF of 81.85%, resulting in an average PCE of 23.59%. Meanwhile, the ATMP–TiO_2 based PSC exhibits a higher average PCE of 24.10% with an average J_{SC} of 24.81 mA cm^{-2}, V_{OC} of 1.19 V and FF of 81.76%. The improved performance of the device with ATMP–TiO_2 is mainly attributed to the increased V_{OC} and J_{SC}, which originated from enhanced energy level alignment and efficient charge collection at the ATMP–TiO_2/perovskite interface. The current density–voltage (J–V) curves of the best performing devices based on different ETLs are shown in Fig. 4e and the corresponding external quantum efficiency (EQE) plots are displayed in Fig. 4f. Both devices show high EQE values exceeding ~90% at a broad wavelength range between 400 and 700 nm, indicating efficient photon acquisition and charge collection in PSCs. The integrated J_{SC} values are 24.60 and 24.89 mA cm^{-2} for PSCs with the control and ATMP-modified TiO_2,

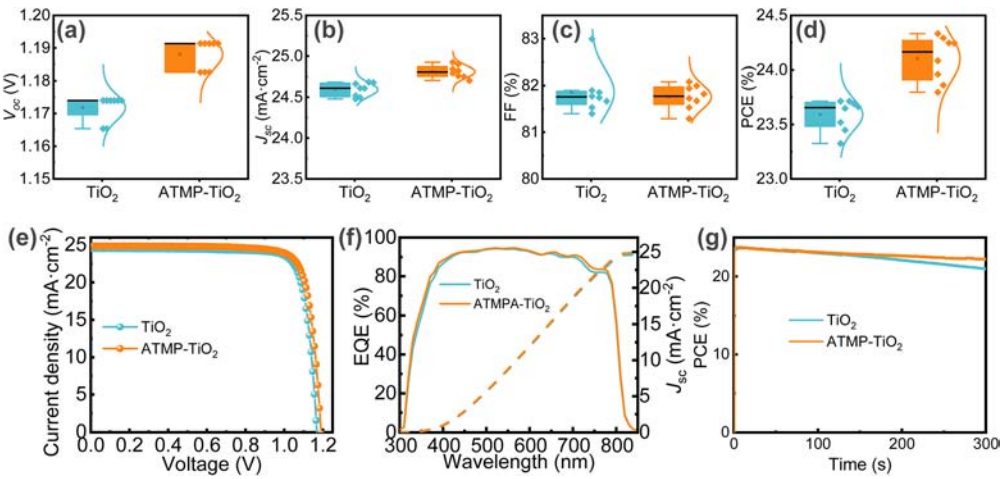

Fig. 4 Statistics distribution box plots of (a) V_{OC}, (b) J_{SC}, (c) FF, and (d) PCE of PSCs with TiO_2 and ATMP–TiO_2 films as ETLs, respectively. The statistics were collected from 8 PSCs. (e) J–V curves of the best performing device based on TiO_2 and ATMP–TiO_2 films. (f) EQE spectra and the integrated J_{SC} of PSCs with TiO_2 and ATMP–TiO_2 as ETLs. (g) MPP of PSCs based on TiO_2 and ATMP–TiO_2 ETLs in ambient air under AM 1.5G illumination.

Table 1 *J–V* parameters of devices with TiO_2 and ATMP–TiO_2 ETLs[a]

ETLs		J_{SC} (mA cm^{-2})	V_{OC} (V)	FF (%)	PCE (%)
TiO_2	Average	24.59 ± 0.08	1.17 ± 0.01	81.85 ± 0.49	23.59 ± 0.14
	Best	24.66	1.17	81.89	23.71
ATMP–TiO_2	Average	24.81 ± 0.08	1.19 ± 0.01	81.76 ± 0.26	24.10 ± 0.21
	Best	24.92	1.19	81.94	24.33

[a] Average results are obtained from 8 devices under each condition.

respectively, which show a negligible difference from the J_{SC} values obtained from the *J–V* scans. We also measured the steady-state efficiency of devices with different TiO_2 ETLs at their maximum power point (MPP) for 300 s (Fig. 4g). The stabilized PCE of the reference device decreases by 11.8% (from 23.7 to 20.9%), while that of the ATMP–TiO_2 based PSC decreases by 6.7% (from 23.8 to 22.2%).

The optical properties and charge dynamics were investigated to further clarify the cause of the difference in the device performance. Both UV-vis absorption spectra of the perovskite deposited on TiO_2 and ATMP–TiO_2 films display broad absorption in the visible light range (Fig. 5a). The steady-state photoluminescence (SSPL) and time-resolved photoluminescence (TRPL) characterization were performed to study the carrier extraction/transport at the ETL/perovskite interface. The SSPL spectra of perovskite layers on TiO_2 and ATMP–TiO_2 ETLs are shown in Fig. 5b. Compared to the control TiO_2/perovskite film, the ATMP–TiO_2/perovskite sample shows lower peak intensity and a much stronger PL quenching effect, suggesting efficient electron extraction and transfer from the perovskite to the ETL. In addition, the normalized TRPL decay spectra (Fig. 5c) were fitted by the biexponential model: $y = A_1 \exp(x/\tau_1) + A_2 \exp(x/\tau_2)$, in which A_1 and A_2 are prefactors, and τ_1 and τ_2 are the lifetimes of the fast and slow decay components, respectively. The average PL lifetime (τ) is determined through the equation: $\tau = (A_1\tau_1^2 + A_2\tau_2^2)/(A_1\tau_1 + A_2\tau_2)$. The fitted results are summarized in Table S1.† The perovskite film deposited on the ATMP-modified ETL exhibits smaller PL lifetimes (0.99 μs) in comparison with the control TiO_2 based sample (1.44 μs), indicating that ATMP regulation leads to faster electron extraction at the cathode.

To look deep into the trap-assisted charge recombination in the device, V_{OC} as a function of light intensity (P_{light}) was investigated. According to the formula: $V_{OC} = nk_BT(\ln P_{light})/q$ + constant, where n is the ideal factor, k_B is the Boltzmann's constant, T is the absolute temperature and q is the elementary charge, V_{OC} exhibits linear correlation with the natural logarithm of P_{light}.[38,39] In principle, smaller the ideal factor, lesser the trap assisted recombination involved in the PSCs. As shown in Fig. 5d, the control device exhibits a slope of 1.56 k_BT/q, while that for the device based on ATMP–TiO_2 is 1.12 k_BT/q, suggesting that the trap-assisted recombination in PSCs with ATMP–TiO_2 has been suppressed, thus resulting in improved V_{OC} and PCE.

To estimate the density of trap states (N_{trap}), we fabricated electron-only devices with the structure of FTO/TiO_2/perovskite/PCBM/Au and FTO/ATMP–TiO_2/perovskite/PCBM/Au. Dark current–voltage characteristics of electron-only devices are

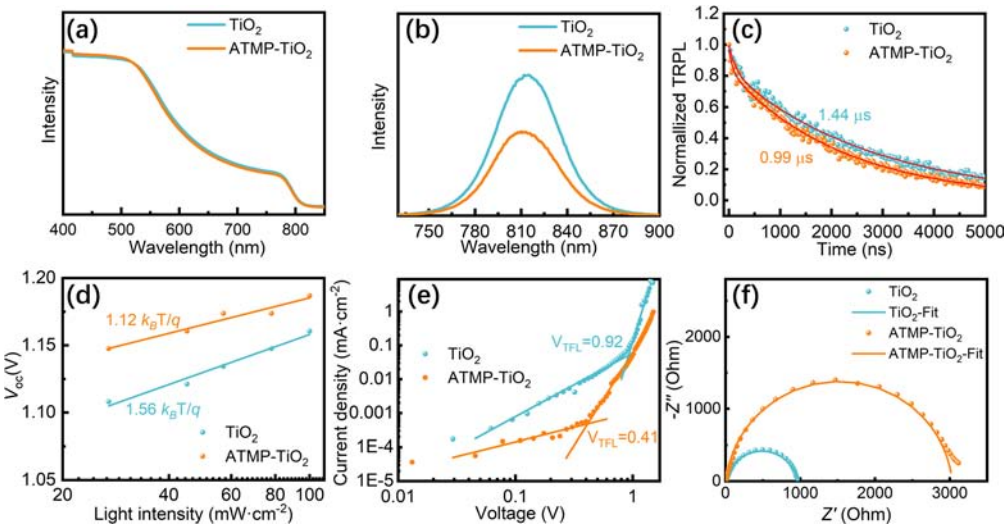

Fig. 5 (a) UV-vis absorption spectra for perovskite films deposited on TiO_2 and ATMP–TiO_2 ETLs. (b) PL spectra of the perovskite deposited on TiO_2 and ATMP–TiO_2. (c) TRPL decay spectra of perovskite deposited on TiO_2 and ATMP–TiO_2. (d) Light-dependent V_{OC} changes for the control and target PSCs. (e) Log–log plot of *J–V* curves with structures of FTO/TiO_2/perovskite/PCBM/Au and FTO/ATMP–TiO_2/perovskite/PCBM/Au in the dark. (f) Nyquist impedance plots for the control and target PSCs with −1 V bias voltage in the dark.

shown in Fig. 5e. The density of the defect is calculated from the equation $V_{TFL} = eL^2N_{trap}/2\varepsilon_0\varepsilon_r$, in which V_{TFL}, e, L, ε_0 and ε_r are the trap-filled limit voltage, elementary charge, thickness of perovskite films, permittivity of vacuum, and dielectric constant of the perovskite, respectively.[40–42] N_{trap} of the ATMP–TiO_2 based electron-only device is estimated to be 7.83×10^{15} cm^{-3}, which is lower than that of the control device (1.76×10^{16} cm^{-3}), suggesting the high conductivity of ETL and well-connected perovskite/TiO_2 interface induced efficient trap passivation.

Furthermore, we conducted electrical impedance spectroscopy (EIS) measurements to further explore the charge transport dynamics in the PSC device. Nyquist impedance plots of the PSCs with control TiO_2 and ATMP–TiO_2 measured at -1 V bias voltage under the dark condition are shown in Fig. 5f. The plots are fitted according to the equivalent circuit inserted in Fig. 5f and the fitting parameters are listed in Table S2.† The PSC based on ATMP–TiO_2 displays a recombination resistance (R_{rec}) of 3022 Ω which is much higher than that of the control TiO_2 based device (948 Ω), suggesting that the ATMP–TiO_2 ETL could enhance the charge transport and suppress the charge recombination at the interface compared to the control TiO_2 ETL.

Conclusions

In summary, we introduced ATMP into the TiO_2 synthesis process to successfully regulate the photoelectric properties of TiO_2 ETLs. With up to six bonding sites on phosphonate groups, ATMP can control the growth of TiO_2 particles through chelation and steric hindrance effect, resulting in efficient TiO_2 ETLs with appropriate band energy and surface morphology. Compared to the control devices, PSCs based on ATMP–TiO_2 deliver a higher average V_{OC} of 1.19 V and PCE of 24.10%. The enhanced performance is ascribed to the better electron capturing properties, lower trap state density and higher recombination resistance at the ATMP–TiO_2/perovskite interface, facilitating efficient carrier extraction and electron transport. Our strategy of using a minute quantity of ATMP to optimize the morphology of the TiO_2 ETL and energy level structure at the ETL/perovskite interface paves an environmental and cost-effective way to improve the efficiency of PSCs.

Experimental details

Materials

F-doped SnO_2 (FTO) glass (12×18 mm, 8 Ω sq^{-1}) was purchased from Youxuan New Energy Technology Co. Ltd (Yingkou, China). Titanium tetrachloride ($TiCl_4$) and amino trimethylene phosphonic acid (ATMP, 50 wt%) were purchased from Aladdin (Shanghai, China). Formamidinium iodide ($CH(NH_2)_2I$, FAI), methylammonium chloride (CH_3NH_3Cl, MACl), cesium iodide (CsI), 4-methoxyphenylethylamine hydroiodide (MeO-PEAI), 4-*tert*-butylpyridine (*t*BP), Li-bis(trifluoromethanesulfonyl)imide (Li-TFSI) and 2,2′,7,7′-tetrakis[*N*,*N*-di(4-methoxy phenyl)amino]-9,9′-spirobifluorene (spiro-OMeTAD) were purchased from Xi'an Polymer Light Technology Corporation. PbI_2, *N*,*N*-dimethylformamide (DMF), dimethyl sulfoxide (DMSO), isopropanol (IPA) and chlorobenzene (CB) were purchased from Thermo scientific. Acetonitrile (ACN) was purchased from Sigma-Aldrich. Anhydrous ether was purchased from Tianjin Jindongtianzheng Precision Chemical Reagent Factory. All chemicals used in this study were used directly without further purification.

Precursor preparation

$TiCl_4$ precursor solution was prepared by diluting 3 mL $TiCl_4$ with 180 mL deionized water. The perovskite precursor solution was prepared by dissolving PbI_2 (0.7420 g), FAI (0.2244 g), MACl (0.0101 g) and CsI (0.0198 g) in 0.8 mL DMF and 0.2 mL DMSO. MeO-PEAI was dissolved in IPA with the concentration of 4.5 mg mL^{-1}. The spiro-OMeTAD solution was prepared by mixing 72.3 mg spiro-OMeTAD, 27 μL 4-tBP and 17.5 μL Li-TFSI solution (520 mg mL^{-1}, in ACN) in 1 mL CB.

Device fabrication

FTO glass substrates were cleaned under ultrasonication sequentially in detergent, ethanol and water for 15 min and then dried with nitrogen. TiO_2 films were prepared as the electron transport layer (ETL) by immersing FTO in 180 mL $TiCl_4$ precursor solution at 70 °C for 5 h. Then, FTO/TiO_2 films were rinsed with deionized water and dried in a stream of nitrogen. As for the preparation of ATMP–TiO_2 films, 50 μL ATMP was added in the $TiCl_4$ precursor solution. The remaining procedure is identical to that of the fabrication of TiO_2 films. The FTO/ETL substrates were kept in an incubator at the temperature of 60 °C and under UV-ozone for 30 min before use. The perovskite precursor was spin-coated onto TiO_2-based films (4000 rpm for 18 s) in a N_2 glove box, and 950 μL diethyl ether was slowly dropped on the film at 12 seconds before the end of spin-coating, followed by annealing at 110 °C for 60 min in air with a humidity of 30–40%. Subsequently, 25 μL MeO-PEAI solution was spin-coated onto the perovskite layer (4000 rpm for 30 s). After that, the films were heated at 100 °C for 3 min. The spiro-OMeTAD solution was spin-coated at 4000 rpm for 30 s without further annealing to generate a hole transport layer. Finally, an Au electrode with a thickness of 70 nm was thermally evaporated onto spiro-OMeTAD films to obtain the solar cell device.

Characterization

Particle-size distribution in the sols was monitored by the technique of dynamic light scattering (DLS, Zetasizer Nano ZS90, Malvern, United Kingdom). XPS spectra were recorded using a Thermo Fisher Scientific ESCALAB 250Xi system equipped with Al K_α radiation. The morphologies of perovskite films were investigated using a HITACHI SU8010 and atomic force microscopy (FMNanoview 1000). The X-ray diffraction (XRD) pattern was obtained using a Rigaku Ultima IV X-ray diffractometer with Cu Kα1(1.54 Å). UV-visible absorption spectra were recorded using a Shimadzu UV-2600 spectrophotometer. Steady-state photoluminescence and time-resolved photoluminescence were studied using a FLS980 fluorescence spectrometer (Edinburgh Instrument). The current density–voltage (*J*–*V*) characteristics of the devices were measured in

darkness and under AM 1.5G illumination (XES-301S + EL-100) using a Keithley 2400 source meter. The light intensity was calibrated to 100 mW cm^{-2} with a standard silicon cell (the KG-5 reference cell). External quantum efficiency (EQE) was measured using QE-R systems (Enli Tech. Hsinchu Taiwan China) in AC mode. Light intensity was adjusted using the standard single-crystal Si photovoltaic cell before the measurement. The back-side of the PSC device was coated with an anti-reflection film during the *J–V* and EQE measurement. The electrochemical impedance spectroscopy (EIS) measurement of PSCs was conducted with a Zahner–Zennium electrochemical workstation.

Author contributions

Xiaopeng Yue and Binging Fan contributed equally to this work.

Conflicts of interest

The authors declare no conflict of interest.

Acknowledgements

This work is supported partially by the National Natural Science Foundation of China (Grant no. 52232008, 51972110, 52102245, and 52072121), Beijing Natural Science Foundation (2222076, 2222077), Beijing Science and Technology Project (Z211100004621010), project of State Key Laboratory of Alternate Electrical Power System with Renewable Energy Sources (LAPS202114), 2022 Strategic Research Key Project of Science and Technology Commission of the Ministry of Education, Huaneng Group Headquarters Science and Technology Project (HNKJ20-H88), the Fundamental Research Funds for the Central Universities (2022MS029, 2022MS028, 2022MS031) and the NCEPU "Double First-Class" Program.

References

1 Z. Xiao, Y. Yuan, Y. Shao, Q. Wang, Q. Dong, C. Bi, P. Sharma, A. Gruverman and J. Huang, *Nat. Mater.*, 2015, **14**, 193–198.
2 M. Liu, M. B. Johnston and H. J. Snaith, *Nature*, 2013, **501**, 395–398.
3 M. Gratzel, *Nat. Mater.*, 2014, **13**, 838–842.
4 S. D. Stranks, G. E. Eperon, G. Grancini, C. Menelaou, M. J. Alcocer, T. Leijtens, L. M. Herz, A. Petrozza and H. J. Snaith, *Science*, 2013, **342**, 341–344.
5 G. Xing, N. Mathews, S. Sun, S. S. Lim, Y. M. Lam, M. Grätzel, S. Mhaisalkar and T. C. Sum, *Science*, 2013, **342**, 344–347.
6 Y. Zhao, F. Ma, Z. Qu, S. Yu, T. Shen, H. X. Deng, X. Chu, X. Peng, Y. Yuan, X. Zhang and J. You, *Science*, 2022, **377**, 531–534.
7 H. Min, D. Y. Lee, J. Kim, G. Kim, K. S. Lee, J. Kim, M. J. Paik, Y. K. Kim, K. S. Kim, M. G. Kim, T. J. Shin and S. Il Seok, *Nature*, 2021, **598**, 444–450.
8 J. J. Yoo, G. Seo, M. R. Chua, T. G. Park, Y. Lu, F. Rotermund, Y. K. Kim, C. S. Moon, N. J. Jeon, J. P. Correa-Baena, V. Bulovic, S. S. Shin, M. G. Bawendi and J. Seo, *Nature*, 2021, **590**, 587–593.
9 M. Kim, J. Jeong, H. Lu, T. K. Lee, F. T. Eickemeyer, Y. Liu, I. W. Choi, S. J. Choi, Y. Jo and H.-B. Kim, *Science*, 2022, **375**, 302–306.
10 E. H. Anaraki, A. Kermanpur, L. Steier, K. Domanski, T. Matsui, W. Tress, M. Saliba, A. Abate, M. Grätzel, A. Hagfeldt and J.-P. Correa-Baena, *Energy Environ. Sci.*, 2016, **9**, 3128–3134.
11 J. H. Heo, H. J. Han, D. Kim, T. K. Ahn and S. H. Im, *Energy Environ. Sci.*, 2015, **8**, 1602–1608.
12 J. Burschka, N. Pellet, S. J. Moon, R. Humphry-Baker, P. Gao, M. K. Nazeeruddin and M. Gratzel, *Nature*, 2013, **499**, 316–319.
13 Q. Jiang, Y. Zhao, X. W. Zhang, X. L. Yang, Y. Chen, Z. M. Chu, Q. F. Ye, X. X. Li, Z. G. Yin and J. B. You, *Nat. Photonics*, 2019, **13**, 460–466.
14 Y. Shang, T. Zhang, D. Yu, Z. Peng, W. Zhou, D. Yin and Z. Ning, *ACS Appl. Mater. Interfaces*, 2021, **13**, 47603–47609.
15 G. Yang, H. Tao, P. Qin, W. Ke and G. Fang, *J. Mater. Chem. A*, 2016, **4**, 3970–3990.
16 H. Zhou, Q. Chen, G. Li, S. Luo, T. B. Song, H. S. Duan, Z. Hong, J. You, Y. Liu and Y. Yang, *Science*, 2014, **345**, 542–546.
17 D. Liu, S. Li, P. Zhang, Y. Wang, R. Zhang, H. Sarvari, F. Wang, J. Wu, Z. Wang and Z. D. Chen, *Nano Energy*, 2017, **31**, 462–468.
18 H. Lu, J. Zhong, C. Ji, J. Zhao, D. Li, R. Zhao, Y. Jiang, S. Fang, T. Liang, H. Li and C. M. Li, *Nano Energy*, 2020, **68**, 104336.
19 C. Liang, Z. Wu, P. Li, J. Fan, Y. Zhang and G. Shao, *Appl. Surf. Sci.*, 2017, **391**, 337–344.
20 X. Huang, Z. Hu, J. Xu, P. Wang, J. Zhang and Y. Zhu, *Electrochim. Acta*, 2017, **231**, 77–84.
21 T. Ye, J. Xing, M. Petrović, S. Chen, V. Chellappan, G. S. Subramanian, T. C. Sum, B. Liu, Q. Xiong and S. Ramakrishna, *Sol. Energy Mater. Sol. Cells*, 2017, **163**, 242–249.
22 H. Huang, P. Cui, Y. Chen, L. Yan, X. Yue, S. Qu, X. Wang, S. Du, B. Liu, Q. Zhang, Z. Lan, Y. Yang, J. Ji, X. Zhao, Y. Li, X. Wang, X. Ding and M. Li, *Joule*, 2022, **6**, 2186–2202.
23 Y. Xu, C. Gao, S. Tang, J. Zhang, Y. Chen, Y. Zhu and Z. Hu, *J. Alloys Compd.*, 2019, **787**, 1082–1088.
24 J. Ma, J. Chang, Z. Lin, X. Guo, L. Zhou, Z. Liu, H. Xi, D. Chen, C. Zhang and Y. Hao, *J. Phys. Chem. C*, 2018, **122**, 1044–1053.
25 H. Zhou, Q. Chen, G. Li, S. Luo, T. B. Song, H. S. Duan, Z. Hong, J. You, Y. Liu and Y. Yang, *Science*, 2014, **345**, 542–546.
26 W. Hu, W. Zhou, X. Lei, P. Zhou, M. Zhang, T. Chen, H. Zeng, J. Zhu, S. Dai, S. Yang and S. Yang, *Adv. Mater.*, 2019, **31**, e1806095.
27 F. Shahvaranfard, M. Altomare, Y. Hou, S. Hejazi, W. Meng, B. Osuagwu, N. Li, C. J. Brabec and P. Schmuki, *Adv. Funct. Mater.*, 2020, **30**, 1909738.
28 C. Tao, S. Neutzner, L. Colella, S. Marras, A. R. Srimath Kandada, M. Gandini, M. D. Bastiani, G. Pace, L. Manna, M. Caironi, C. Bertarelli and A. Petrozza, *Energy Environ. Sci.*, 2015, **8**, 2365–2370.

29 S. A. Paniagua, A. J. Giordano, O. L. Smith, S. Barlow, H. Li, N. R. Armstrong, J. E. Pemberton, J. L. Bredas, D. Ginger and S. R. Marder, *Chem. Rev.*, 2016, **116**, 7117–7158.
30 S. Y. Abate, D.-C. Huang and Y.-T. Tao, *Org. Electron.*, 2020, **78**, 105583.
31 P. V. Kamat, *Chem. Rev.*, 1993, **93**, 267–300.
32 M. F. Mady, A. H. Karaly, S. Abdel-Azeim, I. A. Hussein, M. A. Kelland and A. Younis, *Ind. Eng. Chem. Res.*, 2022, **61**, 9586–9599.
33 L. Zhang and J. M. Cole, *ACS Appl. Mater. Interfaces*, 2015, **7**, 3427–3455.
34 L. Zhang, C. Liu, J. Zhang, X. Li, C. Cheng, Y. Tian, A. K. Jen and B. Xu, *Adv. Mater.*, 2018, **30**, e1804028.
35 Y. Wu, X. Yang, W. Chen, Y. Yue, M. Cai, F. Xie, E. Bi, A. Islam and L. Han, *Nat. Energy*, 2016, **1**, 16148.
36 S. Gharibzadeh, P. Fassl, I. M. Hossain, P. Rohrbeck, M. Frericks, M. Schmidt, T. Duong, M. R. Khan, T. Abzieher, B. A. Nejand, F. Schackmar, O. Almora, T. Feeney, R. Singh, D. Fuchs, U. Lemmer, J. P. Hofmann, S. A. L. Weber and U. W. Paetzold, *Energy Environ. Sci.*, 2021, **14**, 5875–5893.
37 C. Ma, M.-C. Kang, S.-H. Lee, S. J. Kwon, H.-W. Cha, C.-W. Yang and N.-G. Park, *Joule*, 2022, **6**, 2626–2643.
38 S. R. Cowan, A. Roy and A. J. Heeger, *Phys. Rev. B*, 2010, **82**, 245207.
39 C. M. Proctor, M. Kuik and T.-Q. Nguyen, *Prog. Polym. Sci.*, 2013, **38**, 1941–1960.
40 M. J. Li, B. Li, G. Z. Cao and J. J. Tian, *J. Mater. Chem. A*, 2017, **5**, 21313–21319.
41 H. Zhao, S. Wang, M. Sun, F. Zhang, X. Li and Y. Xiao, *J. Mater. Chem. A*, 2018, **6**, 10825–10834.
42 D. Shi, V. Adinolfi, R. Comin, M. Yuan, E. Alarousu, A. Buin, Y. Chen, S. Hoogland, A. Rothenberger, K. Katsiev, Y. Losovyj, X. Zhang, P. A. Dowben, O. F. Mohammed, E. H. Sargent and O. M. Bakr, *Science*, 2015, **347**, 519–522.

